Official journal of the CIOMP 2047-7538
www.nature.com/lsa

ARTICLE Open Access

Tantalum pentoxide: a new material platform for high-performance dielectric metasurface optics in the ultraviolet and visible region

Cheng Zhang[1]✉, Lu Chen[2,3], Zhelin Lin[1], Junyeob Song[2], Danyan Wang[1], Moxin Li[1], Okan Koksal[2], Zi Wang[2,3], Grisha Spektor[4], David Carlson[4], Henri J. Lezec[2], Wenqi Zhu[2,3], Scott Papp[4] and Amit Agrawal[2]✉

Abstract

Dielectric metasurfaces, composed of planar arrays of subwavelength dielectric structures that collectively mimic the operation of conventional bulk optical elements, have revolutionized the field of optics by their potential in constructing high-efficiency and multi-functional optoelectronic systems on chip. The performance of a dielectric metasurface is largely determined by its constituent material, which is highly desired to have a high refractive index, low optical loss and wide bandgap, and at the same time, be fabrication friendly. Here, we present a new material platform based on tantalum pentoxide (Ta_2O_5) for implementing high-performance dielectric metasurface optics over the ultraviolet and visible spectral region. This wide-bandgap dielectric, exhibiting a high refractive index exceeding 2.1 and negligible extinction coefficient across a broad spectrum, can be easily deposited over large areas with good quality using straightforward physical vapor deposition, and patterned into high-aspect-ratio subwavelength nanostructures through commonly-available fluorine-gas-based reactive ion etching. We implement a series of high-efficiency ultraviolet and visible metasurfaces with representative light-field modulation functionalities including polarization-independent high-numerical-aperture lensing, spin-selective hologram projection, and vivid structural color generation, and the devices exhibit operational efficiencies up to 80%. Our work overcomes limitations faced by scalability of commonly-employed metasurface dielectrics and their operation into the visible and ultraviolet spectral range, and provides a novel route towards realization of high-performance, robust and foundry-manufacturable metasurface optics.

Introduction

Recent years have witnessed rapid development in the field of all-dielectric metasurfaces, characterized by high operational efficiency and ease of transmission-mode operation, for spatiotemporal shaping of optical fields in a compact and integration-friendly platform[1–10]. Researchers have demonstrated a series of high-performance metasurface devices operating all the way from the terahertz up to the visible and ultraviolet (UV) frequencies using a range of dielectric materials with different bandgaps[11–16]. These devices have found diverse applications in imaging[17–20], displaying[21–24], sensing[25–27], quantum optics[28–30], and more. For metasurfaces operating from the near-infrared to the terahertz region, silicon (Si) has been routinely used thanks to the mature and widely-accessible nanofabrication technologies enabled by the Complementary Metal-Oxide-Semiconductor (CMOS) processes built around Si[31–33]. For devices operating in the visible, silicon nitride (SiN_x)[34–36], gallium nitride (GaN)[37,38], and titanium dioxide (TiO_2)[39–41] have been employed. High-aspect-ratio subwavelength nanostructures of these

Correspondence: Cheng Zhang (cheng.zhang@hust.edu.cn) or Amit Agrawal (amit.agrawal@nist.gov)
[1]School of Optical and Electronic Information & Wuhan National Laboratory for Optoelectronics, Huazhong University of Science and Technology, Wuhan, Hubei 430074, China
[2]National Institute of Standards and Technology, Gaithersburg, MD 20899, USA
Full list of author information is available at the end of the article
These authors contributed equally: Cheng Zhang, Lu Chen

materials are fabricated by either a dedicated reactive ion etch (RIE) process, or a resist-based Damascene process incorporating low-temperature atomic layer deposition (ALD). For metasurface optics operating in the UV, wide-bandgap dielectrics, such as hafnium oxide (HfO_2), niobium pentoxide (Nb_2O_5), and aluminum nitride (AlN), are the common materials of choice. Recently, ALD-based Damascene processes have been further developed to implement high-efficiency UV metasurfaces made of hafnium oxide (HfO_2)[42] or niobium pentoxide (Nb_2O_5)[43], to overcome limitations of RIE recipes employed for patterning these wide-bandgap dielectrics. AlN has been proposed for UV metasurfaces in numerical studies[44] and experimental demonstrations using micron-scale zone-plate-like structures[45] – however, its potential as a viable platform for UV metasurface optics remains to be exploited, as additional investigation is required to pattern AlN into high-aspect-ratio, subwavelength nanostructures with well-controlled sidewall profiles.

In addition to wide-bandgap dielectrics, several alternative material platforms have also been proposed for UV meta-optics. Examples include zirconium dioxide (ZrO_2) nanoparticle embedded UV-curable resin[46] and Van der Waals materials[47–50]. By dispersing ZrO_2 nanoparticles in a UV-curable resin through a proper chemical synthesis process, researchers are able to obtain a new type of imprint resist with a wide bandgap and high refractive index over a broad UV range. Van der Waals materials, such as boron nitride (BN), exhibit high refractive index and broadband optical transparency over the visible and ultraviolet regions, and have been exploited for constructing different excitonic, nanophotonic, and quantum devices. Unfortunately, the materials' distinctive flake-like morphology might impose severe limitations on their applicability for large-scale devices. Furthermore, their pronounced anisotropic optical responses, while offering an additional dimension for device design, may also introduce challenges within the context of typical metasurface applications. Implementing metasurfaces operating over even shorter wavelength regions that lack materials for transmissive optics, such as vacuum UV (VUV) and extreme UV (EUV), is challenging and an active field of study. Demonstrated endeavors include nonlinear signal generation through dielectric metasurfaces[51,52], photon nanosieves in opaque metallic films[53], and vacuum guiding by holes in a silicon membrane[54].

Realization of efficient dielectric metasurfaces involves shaping high-refractive-index and low-loss dielectric materials into high-aspect-ratio subwavelength nanostructures with well controlled shape, size, and orientation. The performance of a dielectric metasurface is largely determined by its constituent material. An ideal material should have a high refractive index (e.g., $n > 2.0$) and large bandgap (E_g) that facilitate lossless operation at short wavelengths, and at the same time, be patternable into high-aspect-ratio nanostructures using standard CMOS processes with straight and smooth sidewall profiles that guarantee accurate realization of the designed structure. Among commonly employed dielectric materials for metasurfaces, Si can be easily patterned into nanostructures of various geometries, but its narrow bandgap ($E_g \approx 1.1$ eV) largely limits operational wavelength down to the near-infrared spectral region. For lossless operation at shorter wavelengths, such as in the visible region, alternative dielectrics such as SiN_x, GaN and TiO_2 have been employed. However, their high-quality films are typically grown by certain chemical vapor deposition (CVD) processes using combination of various precursors and the associated nanopatterning techniques are relatively complicated, involving either a carefully developed RIE or Damascene process. For UV and deep-UV regions, wide-bandgap dielectrics such as Nb_2O_5 and HfO_2 are chosen, whose high-aspect-ratio nano-patterning has so far been limited only to the low-temperature-ALD based Damascene process. However, metasurfaces fabricated by ALD-based Damascene processes are not CMOS-compatible and therefore not commercially feasible, largely limiting their scalability. A comparison of different candidate materials is elaborated in Section I, Supplementary Information.

Here, we demonstrate a new dielectric metasurface platform based on tantalum pentoxide (Ta_2O_5). We implement high-performance UV and visible metasurface optics through commonly-available physical vapor deposition (PVD) and RIE processes that overcome the reliance of standard dielectric materials on the Damascene process as discussed above. The choice of Ta_2O_5, the high-refractive-index component of dielectric mirrors used in the Laser Interferometer Gravitational-Wave Observatory (LIGO)[55], is justified by (*i*) its wide bandgap $E_g \approx 4.0$ eV (corresponding to a free-space wavelength $\lambda_0 = 309$ nm) that enables low-loss metasurface operation across the whole visible and near-UV spectrum, and a part of the mid-UV region; and (*ii*) the ability to pattern it into high-aspect-ratio nanostructures using common fluorine-based RIE processes. The large nonlinear optical coefficients of Ta_2O_5, which can be further enhanced by doping with other dielectrics such as Nb_2O_5[56], have recently been leveraged for frequency comb generation and optical parametric oscillators in optical micro-resonators[57,58], and offer a pathway towards the realization of nonlinear metasurfaces for harmonic generation, optical switching and modulation, as well as quantum information processing.

We deposit high-quality, UV- and visible-transparent Ta_2O_5 films using a reactive magnetron sputtering process and pattern the films into high-aspect-ratio

nanostructures through a fluorine-gas-based RIE process. We implement a series of high-efficiency UV and visible metasurfaces offering a set of representative light-field modulation functionalities. We first show a group of UV metalenses with different numerical apertures (NAs) ranging from 0.5 to 0.7, which are made of Ta_2O_5 nanopillars of circular in-plane cross-sections and exhibit polarization-insensitive focusing capability down to the diffraction limit. The metalenses demonstrate experimentally measured focusing efficiencies up to ≈65% at an operational wavelength of 325 nm. We then realize broadband UV and visible meta-holograms, which are made of Ta_2O_5 nanopillars of elliptical in-plane cross-sections and provide spin-selective holographic projection across the near-UV and blue region. The devices exhibit peak operational efficiencies exceeding 70% at 325 nm. We further demonstrate a series of structural color generating metasurfaces made of resonant Ta_2O_5 nanopillars supporting geometrical Mie resonances. The devices produce bright and high-purity reflection colors across the entire visible region, with measured peak efficiencies of ≈80%. Our work provides a novel route towards robust and low-cost fabrication of high performance dielectric metasurfaces operating in the UV and visible regions using CMOS compatible processes, and promotes realization of compact-form-factor and multifunctional photonic systems based on flat optical elements in these critical spectral regions.

Results

Material preparation and nanostructure fabrication

Ta_2O_5 films are deposited through a radiofrequency (RF) magnetron sputtering process using a Ta_2O_5 target (Fig. 1a). Inset shows the picture of a 400-nm-thick Ta_2O_5 film deposited on a 50-mm-diameter fused silica substrate. Film thickness and refractive index are both characterized by spectroscopic ellipsometry, as detailed in the Materials and Methods section. Although Ta_2O_5 has an intrinsic wide bandgap, films deposited using conventional magnetron sputtering would inevitably have defects, and thus, exhibit sub-bandgap absorption (Fig. 1b, magenta curves). To solve this issue, we develop a reactive RF sputtering process with Oxygen (O_2) gas. As the flow rate of O_2 gas increases, the sputtered Ta_2O_5 film exhibits a monotonically decreasing absorption coefficient k over the UV and visible regions (Fig. 1b, orange and blue curves). With an O_2 flow rate of 2 standard cubic centimeters per minute (sccm), the deposited Ta_2O_5 film exhibits a refractive index $n > 2.27$ over the entire UV range, as well as negligible absorption coefficient k down to $\lambda_0 \approx 300$ nm. Further increase of the O_2 flow rate does not lead to any noticeable change in the refractive indices of the obtained films. It is worth noting that our developed film deposition process does not require any special substrate (e.g., for lattice matching), or heating (cooling) of the substrate during film deposition, therefore enabling a straightforward and high-throughput deposition of high optical quality Ta_2O_5 films onto various types of substrates at room temperature. Although Ta_2O_5 films are deposited using magnetron sputtering process in this study, other PVD processes (e.g., thermal evaporation, electron beam evaporation, pulsed laser deposition, etc.) as well as ALD can be utilized for high-quality Ta_2O_5 film preparation.

The metasurface optics fabrication (Fig. 1c) starts with depositing Ta_2O_5 film of target thickness onto a 500-μm-thick fused silica substrate using the developed reactive sputtering process. Then, a 200-nm-thick layer of positive electron beam resist is spin-coated onto the film, followed by evaporating a 20-nm-thick anti-charging aluminum (Al) layer. A 100 keV electron beam lithography system is used to expose the nanostructure patterns, followed by Al layer removal with diluted tetramethylammonium hydroxide (TMAH) and resist development with hexyl acetate at 4 °C. The developed patterns in the resist layer are transferred to an evaporated 50-nm-thick aluminum oxide (Al_2O_3) layer through a lift-off process. Using the nanostructured Al_2O_3 layer as the etch mask, inductively coupled-plasma reactive ion etching (ICP-RIE, gas mixture: C_4F_8 and O_2; ICP power: 2000 W; RF power: 15 W) is performed to pattern the underlying Ta_2O_5 layer at 50 °C and create high-aspect-ratio Ta_2O_5 nanopillars. The metasurface optics fabrication concludes with soaking the sample in a mixture of hydroperoxide and ammonia hydroxide solutions heated at 80 °C for 30 minutes, to remove the Al_2O_3 etch mask and any etch residue.

Representative scanning electron micrographs (SEMs) of fabricated Ta_2O_5 nanopillars are displayed in Fig. 1d to f, showing straight and smooth sidewall profiles. Patterns with different geometric shapes and sizes, frequently used in a plethora of dielectric metasurface devices, are chosen to illustrate the versatility of the developed fabrication process. In addition, Fig. 1d and e correspond to etching situations with large open (exposed) areas, while Fig. 1f corresponds to situations with small open areas. Figure 1d shows a group of high-aspect-ratio (≈10:1) Ta_2O_5 nanopillars with circular (symmetric) in-plane cross-sections, which are frequently used to construct dielectric metasurfaces with polarization-independent response. Figure 1e shows an array of Ta_2O_5 nanopillars with an even higher aspect ratio (≈12:1), which exhibit rectangular (asymmetric) in-plane cross-sections. Different from the symmetric Ta_2O_5 nanopillars, these structures are typically employed for metasurfaces with polarization-dependent (e.g., linear-polarization-multiplexed, spin-multiplexed, spin-selective, etc.) responses. Figure 1f shows an array of closely packed Ta_2O_5 nanopillars with a

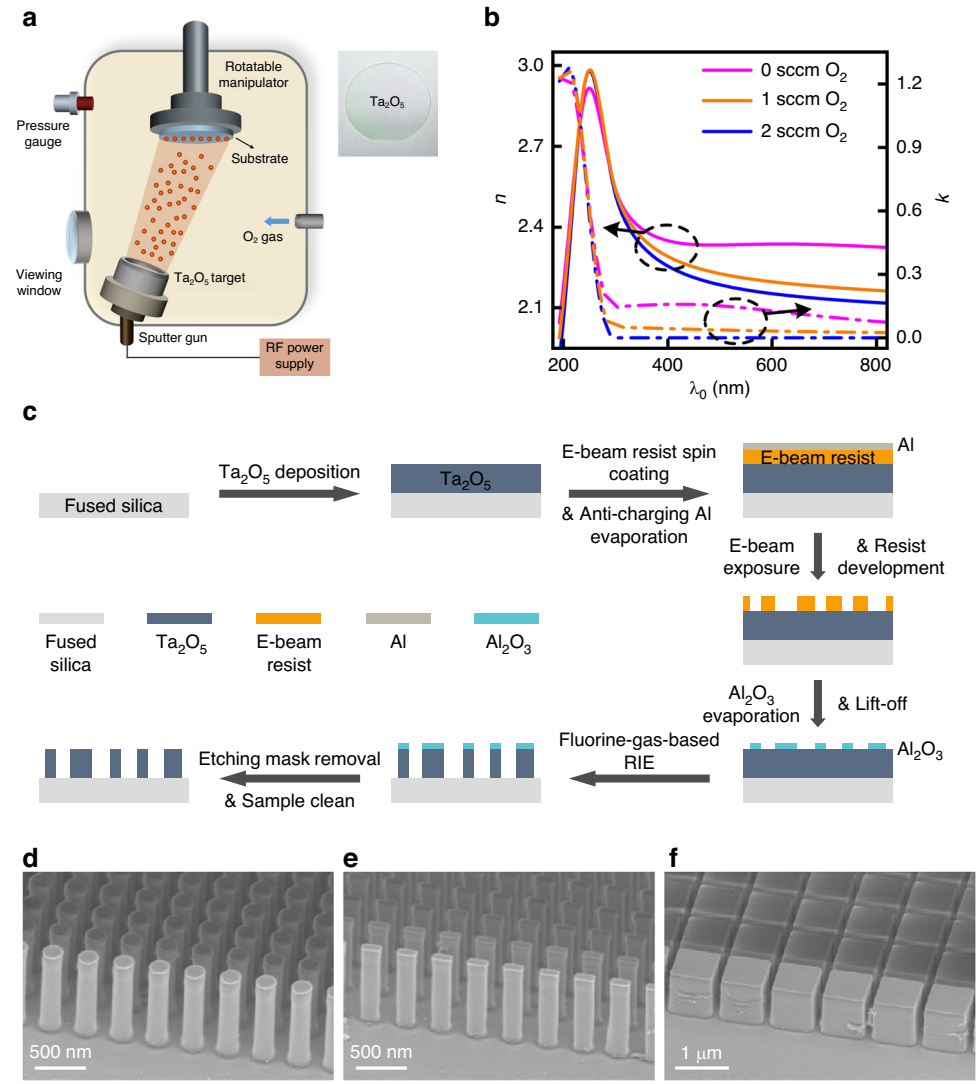

Fig. 1 Material preparation and nanostructure fabrication. a Schematic representation of the O_2-gas-based RF reactive magnetron sputtering process for Ta_2O_5 film deposition. Inset: Photo of a 400-nm-thick Ta_2O_5 film deposited on a 50-mm-diameter fused silica substrate. **b** Refractive index n and extinction coefficient κ of the sputter-deposited Ta_2O_5 films with different O_2 gas flow rates, characterized by spectroscopic ellipsometry. **c** Fabrication flow chart of the Ta_2O_5 metasurface optics, whose key steps include film deposition using the developed sputtering recipe, electron beam lithography, Al_2O_3 etching mask lift-off, and fluorine-gas-based RIE. **d**–**f** Scanning electron micrographs (SEMs) of details of fabricated Ta_2O_5 nanopillars with different geometric shapes

moderate aspect ratio. These structures can be used to create dielectric Mie resonators for spectral filtering, local optical field enhancement, nonlinear harmonic generation, etc.

Polarization-independent UV metalenses

To demonstrate the versatility of this material platform and the developed nanopatterning technique, we choose to implement two different categories of metasurfaces for UV light wavefront shaping respectively based on propagation phase[31,59] and geometric phase[39,60], which are the two most representative wavefront control methods currently employed by dielectric metasurfaces.

The propagation-phase-based metasurface consists of a square lattice of Ta_2O_5 cylindrical nanopillars, where the diameter of each pillar varies as a function of its spatial position on the metasurface plane (Fig. 2a). Each nanopillar acts as a truncated dielectric waveguide with top and bottom interfaces of low reflectivity, through which light propagates with a transmittance T and phase shift φ controlled by the pillar height H, pillar diameter D, and lattice spacing P. Due to the symmetric nature of the

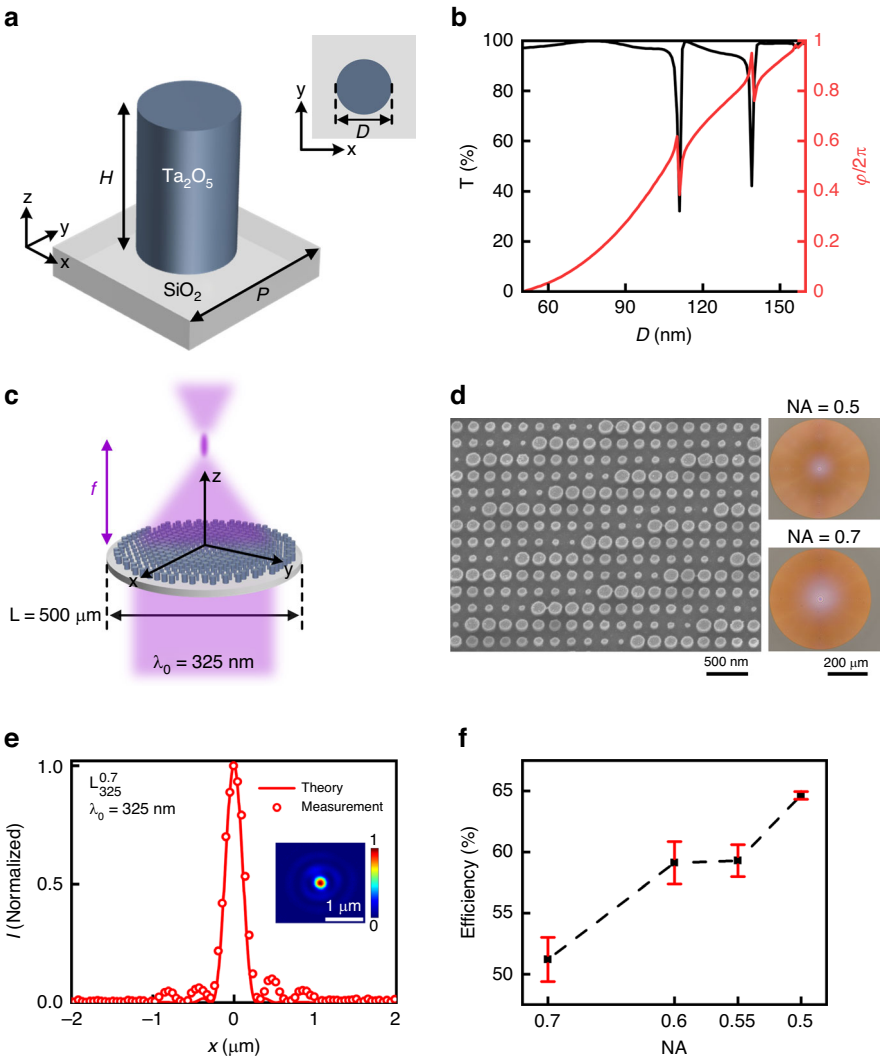

Fig. 2 Polarization-independent UV metalenses. a Schematic representation of a polarization-independent metasurface unit cell, consisting of a high-aspect-ratio Ta_2O_5 circular pillar of height H and cross-sectional diameter D, arranged on a SiO_2 substrate to form a square lattice with subwavelength lattice spacing P. **b** Transmission intensity T and phase shift φ for an incident light of free-space wavelength $\lambda_0 = 325$ nm, as a function of pillar diameter D. A corresponding pillar height ($H = 340$ nm), lattice spacing ($P = 200$ nm), and a range of pillar diameters ($D \in [50, 160]$ nm) are chosen. For ease of display, the phase shift for pillar of diameter $D = 50$ nm is set to zero. **c** Schematic representation of focusing by a polarization-independent, 500-μm-diameter metalens under normal-incidence, plane-wave illumination at $\lambda_0 = 325$ nm. **d** Left panel: Top-view SEM image of a fabricated NA = 0.5 metalens $L^{0.5}_{325}$, consisting of cylindrical Ta_2O_5 nanopillars of varying diameters. Right panel: Optical micrographs of a NA = 0.5 metalens ($L^{0.5}_{325}$, upper part) and a NA = 0.7 metalens ($L^{0.7}_{325}$, lower part). **e** Intensity distribution at the focal plane along the x-axis (dots), measured for metalens $L^{0.7}_{325}$. Theoretical prediction (line) is shown for comparison. Inset: Intensity distribution at the focal plane. **f** Measured focusing efficiency as a function of metalens numerical aperture (NA). Error bars denote two standard deviations of the measured data

nanopillar's in-plane cross-section, propagation phase is independent of incident light polarization. To design the metasurface, the transmittance, T, and induced phase shift, φ, of an array of cylindrical Ta_2O_5 pillars of diameter D, height H, and lattice spacing P, under plane-wave normal incidence illumination at the target operational free-space wavelength $\lambda_0 = 325$ nm, are computed using finite-difference-time-domain (FDTD) simulations with periodic boundary conditions. After several rounds of iteration, a pillar height ($H = 340$ nm) and subwavelength lattice spacing ($P = 200$ nm) is chosen, along with a range of pillar diameters ($D \in [50, 160]$ nm) that yield phase shifts varying over a full range from 0 to 2π, while maintaining a relatively high and constant transmittance for incident light at $\lambda_0 = 325$ nm (Fig. 2b).

Using the obtained nanopillar library, we implement a series of metalenses with numerical aperture (NA) values ranging from 0.5 to 0.7. Four 500-μm-diameter metalenses,

$L_{325}^{0.5}$, $L_{325}^{0.55}$, $L_{325}^{0.6}$, and $L_{325}^{0.7}$, are all designed to focus UV light of $\lambda_0 = 325$ nm (Fig. 2c), but with different NA values of 0.5, 0.55, 0.6, and 0.7, respectively. The associated focal lengths, $f_{325}^{0.5}$, $f_{325}^{0.55}$, $f_{325}^{0.6}$, and $f_{325}^{0.7}$, are 433 μm, 379.6 μm, 333.3 μm, and 255 μm, respectively. Singlet-mode focusing of a normally-incident plane wave can be achieved by implementing a radially-symmetric phase shift function $\varphi^L(x,y,\lambda_0) = \mathrm{mod}\left((2\pi/\lambda_0)\left(f - \sqrt{x^2+y^2+f^2}\right), 2\pi\right)$ over the metasurface plane. Here, f is the focal length, x and y are in-plane distances along orthogonal directions from the centre of the lens, given incident light propagating along the z-direction.

The left panel of Fig. 2d shows the SEM image of the details of a fabricated NA = 0.5 metalens $L_{325}^{0.5}$, consisting of cylindrical nanopillars with spatially varying diameters. The right panel of Fig. 2d displays the optical micrographs of a NA = 0.5 metalens ($L_{325}^{0.5}$, upper part) and a NA = 0.7 metalens ($L_{325}^{0.7}$, lower part). The metalenses are characterized using a custom-built optical setup (detailed in the Materials and Methods section). For each metalens, the measured intensity distribution at the device's focal plane reveals a circularly-symmetric focal spot, characterized by a cross section that closely matches the intensity distribution theoretically predicted for a diffraction-limited lens with certain NA, given by the Airy disk function $I(x) = [2J_1(A)/A]^2$, where J_1 is the first-order Bessel function of the first kind, and $A = 2\pi(\mathrm{NA})x/\lambda_0$ (Fig. 2e and Fig. S2, Supplementary Information). The focusing efficiencies, defined as the ratio of the optical power of the focused spot to the total power illuminating the metalens, are measured to be (64.7 ± 0.3)% ($L_{325}^{0.5}$), (59.3 ± 1.3)% ($L_{325}^{0.55}$), (59.1 ± 1.7)% ($L_{325}^{0.6}$), and (51.2 ± 1.8)% ($L_{325}^{0.7}$). The cited uncertainties represent two standard deviations of the measured data. The metalens efficiency exhibits a slow and monotonical decrease as the device's NA increases (Fig. 2f). These obtained efficiencies are comparable to those of HfO_2-based UV metalenses, which are fabricated through a resist-based Damascene process[42].

Spin-selective and broadband metaholograms

We also implement geometric-phase-based metasurfaces for spin-selective hologram projection, which operate over a broad UV and visible spectrum under left-handed circularly polarized (LCP) light illumination. The geometric-phase-based metasurface consists of a square lattice of Ta_2O_5 elliptical nanopillars shaped identically, but with spatially-varying rotation angles (Fig. 3a). Each nanopillar acts as a miniaturized half-waveplate for incident circularly-polarized light, and transmits with circular polarization of opposite handedness along with a phase delay that equals twice the pillars' rotation angle. Such phase modulation is typically referred to as the Pancharatnam-Berry (PB) phase or geometric phase[60]. To design the geometric-phase-based metasurface operating at $\lambda_0 = 325$ nm, the transmittance and phase shift for propagation of 325 nm wavelength light, linearly-polarized either (*i*) parallel to the major axis (T_1 and Δ_1), or (*ii*) parallel to the minor axis (T_2 and Δ_2) of an array of elliptical Ta_2O_5 nanopillars are computed using FDTD simulations with periodic boundary conditions. For a chosen pillar height $H = 380$ nm and lattice spacing $P = 270$ nm, the major and minor axis lengths of the pillar, D_1 and D_2, are iteratively varied to identify orthogonal principal axis combinations simultaneously leading to $|\Delta_1 - \Delta_2| \approx \pi$ and $T_1 \approx T_2$, in other words, half-waveplate-like operation. To facilitate the above parameter search process, a figure-of-merit (FoM) function is defined as $\mathrm{FoM} = \log_{10}\left(\left|\frac{T_1}{T_2}e^{(i(\Delta_1-\Delta_2))} - e^{i\pi}\right|\right)$ and displayed in Fig. 3b, where the blue-colored regions (i.e., low-FoM value regions) correspond to various combinations of D_1 and D_2 that satisfy the target half-waveplate operation. The chosen pillar geometry in this study ($D_1 = 200$ nm and $D_2 = 76$ nm) is denoted by a red star.

The implemented metahologram (denoted H_{325}^{LCP}), which occupies a square area with a side length of 540 μm, is mapped to a Cartesian coordinate system where the constituent metasurface is in the $z = 0$ plane and the 1st x-y quadrant, with one corner positioned at the origin (Fig. 3c). The metahologram operates by converting a left-handed circularly polarized (LCP) incident light into a right-handed circularly polarized (RCP) light upon transmission, and at the same time, imparting a spatially-varying phase shift modulation onto the transmitted light for the subsequent holographic image formation. The Gerchberg-Saxton (GS) algorithm[61] is employed to calculate the phase shift profiles, $\varphi_{325}^H(x,y,\lambda_0)$, required to project a holographic "Ta_2O_5 UV" image (4 mm in width) located in the $z = 40$ mm plane, under normally-incident plane-wave illumination of $\lambda_0 = 325$ nm (Fig. S3, Supplementary Information). An additional offset of $y = -3$ mm is added to avoid overlap of the generated holographic image with the residual directly transmitted beam.

The SEM image of the fabricated metahologram H_{325}^{LCP} is displayed in Fig. 3d. The sample is characterized using a custom-built imaging system (detailed in the Materials and Methods section). The measured image projected by the device under $\lambda_0 = 325$ nm illumination is displayed in the middle panel of Fig. 3e, which faithfully replicates the shape of the corresponding target image (left panel, Fig. 3e) numerically computed assuming an ideal metahologram realization with both the designed phase shift profile $\varphi_{325}^H(x,y,\lambda_0)$ and unity transmittance T. The measured efficiency, defined as the ratio of the total optical power of the holographic image to the total power illuminating the

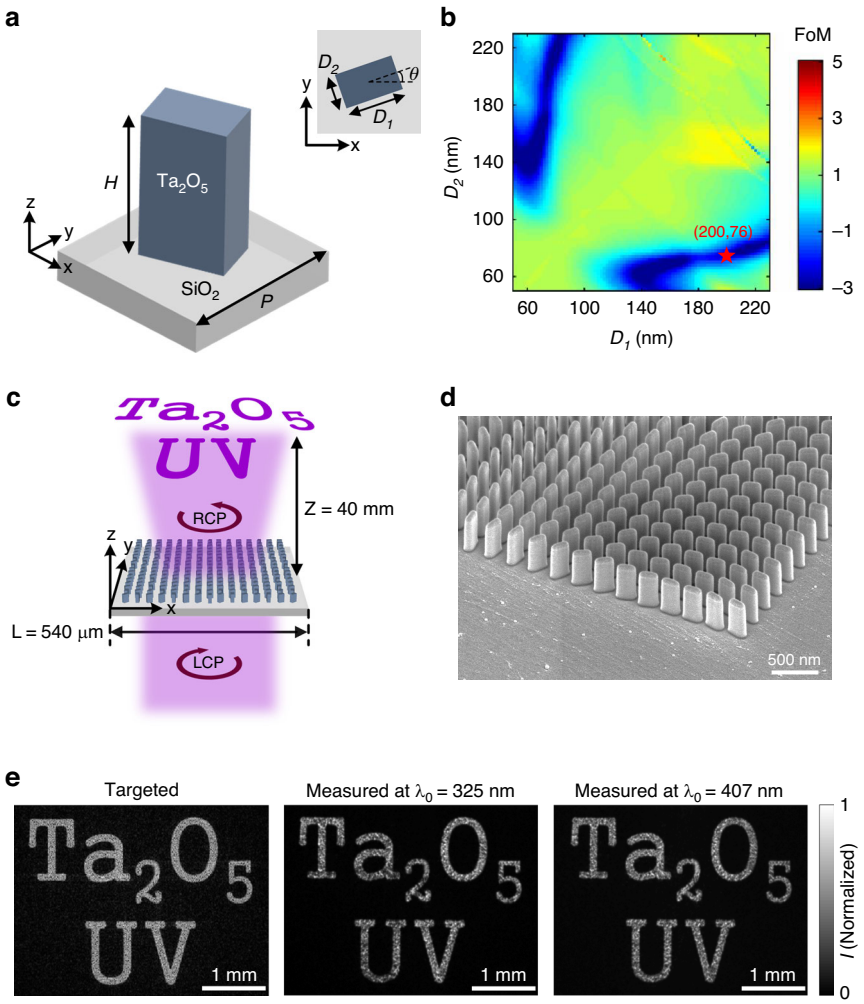

Fig. 3 Spin-selective and broadband metaholograms. a Schematic representation of a spin-selective metasurface unit cell, consisting of a high-aspect-ratio Ta_2O_5 cylindrical pillar of height H, with an elliptical cross-section (major and minor axis lengths of D_1 and D_2, respectively), and rotation angle θ arranged on a SiO_2 substrate to form a square lattice with subwavelength lattice spacing P. Spin-selective optical field modulation can be implemented via the variation of D_1, D_2, and θ as a function of nanopillar position within the lattice. **b** Half-waveplate figure of merit (FoM) versus nanopillar in-plane dimensions (D_1 and D_2) at target free-space wavelength $\lambda_0 = 325$ nm, where the blue-colored regions (i.e., low-FoM value regions) correspond to various combinations of D_1 and D_2 that satisfy the half-waveplate-like operation. Pillar height $H = 380$ nm and lattice spacing $P = 270$ nm are used during the calculation. The chosen pillar geometry in this study ($D_1 = 200$ nm and $D_2 = 76$ nm) is denoted by a red star. **c** Schematic representation of the holographic image projection by a spin-selective metahologram, H_{325}^{LCP}, under normal-incidence, left-handed circularly polarized (LCP) plane-wave illumination at $\lambda_0 = 325$ nm. **d** SEM of details of a fabricated metahologram H_{325}^{LCP}, consisting of elliptical Ta_2O_5 nanopillars of varying rotation angles. Viewing angle: 52°. **e** Targeted (left panel) and measured (middle and right panels) holographic images projected by the metahologram H_{325}^{LCP} in the $z = 40$ mm plane. The targeted image is numerically computed assuming an ideal metahologram realization with both the designed phase shift profile $\varphi_{325}^{H}(x, y, \lambda_0)$ and unity transmittance T, under normal-incidence illumination at $\lambda_0 = 325$ nm

structure, is (75.9 ± 1.1)%. The cited uncertainty represents two standard deviations of the measured data. The obtained efficiency value is comparable to those of recently reported TiO_2-based metaholograms operating in the visible[39], and HfO_2-based devices operating in the UV[42]. The broadband characteristic of the employed geometric phase and absorption-free nature of Ta_2O_5 across the UV and visible regions, allow the metahologram to operate over a wide wavelength range. We experimentally characterize device performance under an LCP laser beam illumination at $\lambda_0 = 407$ nm. The captured holographic image (right panel, Fig. 3e) closely resembles the target image displayed in the left panel of Fig. 4e, with a measured efficiency of (37.3 ± 0.3)%.

Structural color generating metasurfaces

The deposited Ta_2O_5 films exhibit a high refractive index and negligible extinction coefficient at wavelengths

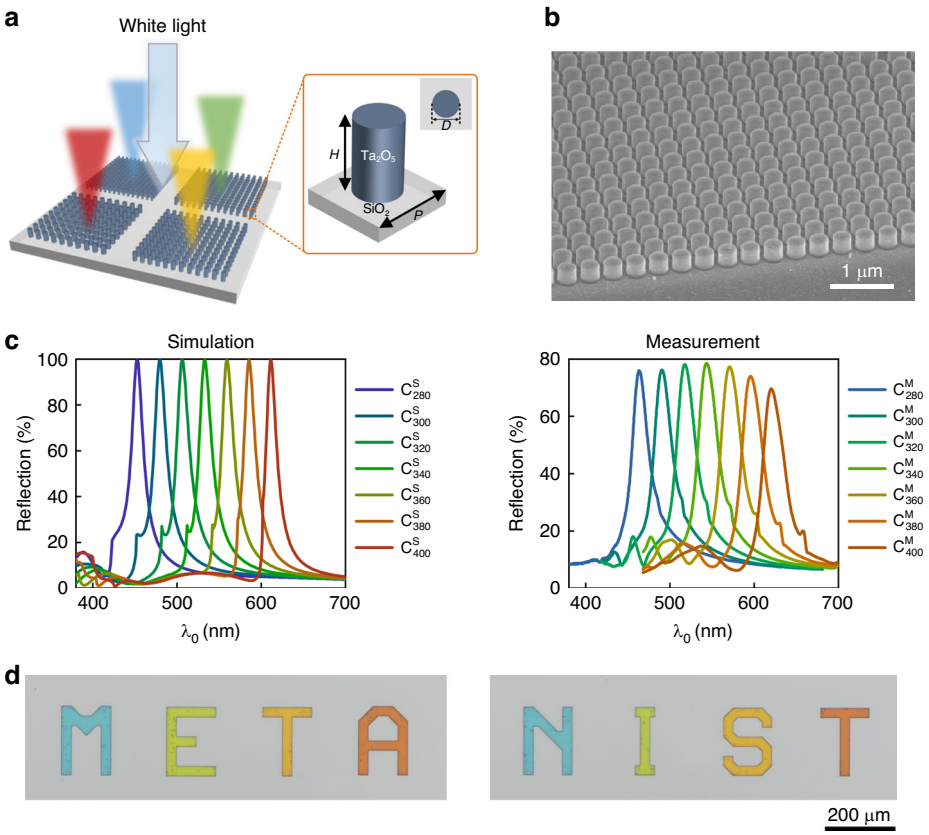

Fig. 4 Structural color generating metasurfaces. a Schematic representation of the reflection-mode structural color generation by an array of Ta_2O_5 Mie resonators, under normal-incidence white light. Inset: Schematic illustration of a Ta_2O_5 Mie resonator unit cell, consisting of a Ta_2O_5 circular pillar of height *H* and cross-sectional diameter *D*, arranged on a SiO_2 substrate to form a square lattice with subwavelength lattice spacing *P*. By fixing the pillar height (*H*) as 240 nm and filling ratio ($f = D/P$) as 0.7 and varying the pillar lattice spacing (*P*) from 260 nm to 400 nm, different reflection colors covering the full visible range are created. **b** SEM image of a fabricated structural color generating metasurface of lattice spacing of 300 nm (C_{300}), consisting of cylindrical Ta_2O_5 nanopillars with circular cross-sections, of uniform sizes and straight side-wall profiles. Viewing angle: 54°. **c** Simulated (left panel) and measured (right panel) reflection spectra of seven structural color generating metasurfaces with different lattice spacings. For each curve, the employed color is deliberately chosen according to the standard RGB values calculated from the associated reflection spectrum and indicates the perceived color by human eye. **d** Optical micrographs of colored words "META" and "NIST" printed by the Ta_2O_5 metasurfaces

longer than 300 nm, the material's bandgap. As observed in Fig. 1b, the 2 sccm O_2-deposited Ta_2O_5 is free of optical absorption and simultaneously displays a refractive index $n > 2.12$ over the whole visible range (380 nm to 750 nm). This offers a promising material platform for realizing high-performance metasurface devices operating in the visible spectrum, thus far achieved using other materials such as TiO_2, SiN_x and GaN.

We implement structural color generation based on Ta_2O_5 Mie resonators as a demonstration of high-performance metasurfaces at visible wavelengths. Figure 4a depicts the schematic of the Ta_2O_5-based structural color generating metasurface, which consists of a square lattice of Ta_2O_5 cylindrical nanopillars with height *H* and diameter *D*, arrayed over a lattice spacing *P* on fused silica substrate. Mie resonances[62–64] are supported by the high-refractive-index Ta_2O_5 nanopillars, generating distinct spectral peaks in reflection. The central wavelength of the reflection peak (i.e., the generated reflection color) can be adjusted by varying one or several geometric parameters of the nanopillar, such as its height, diameter, or lattice spacing. In our design, we fix the pillar height (*H*) as 240 nm, and the pillar filling ratio ($f = D/P$) as 0.7. By varying the lattice spacing (*P*) from 260 nm to 400 nm, different reflection colors covering the full visible range are created (Left panel, Fig. 4c). Moreover, the generated colors exhibit narrow spectral widths (indicating high color purity), and at the same time, peak reflection intensities of up to 100% (indicating high color brightness). In the figure, the employed color for each curve is deliberately chosen according to standard RGB (sRGB) values calculated from the associated reflection spectrum and indicates colors perceived by the human eye. Angular response of the designed color generating

metasurface and ways to tune its spectral linewidth are respectively elaborated in Section IV and V, Supplementary Information.

Seven 500-μm-square-area Ta_2O_5 metasurfaces (C_{280}, C_{300}, C_{320}, C_{340}, C_{360}, C_{380}, and C_{400}) of lattice spacing varying from 280 nm to 400 nm with a step size of 20 nm, are fabricated and characterized. A representative SEM image of a 300 nm period sample, C_{300}, is displayed in Fig. 4b, showing pillars of uniform sizes and straight sidewall profiles. Measured reflection spectra of the fabricated samples are plotted in the right panel of Fig. 4c. Similarly, the color of each curve is chosen based on the sRGB values calculated from the corresponding measured reflection spectrum. The simulated and measured reflection spectra agree well, in terms of both the line shape and perceived color. For all obtained samples, the peak reflection intensities are close to ≈80%, which is comparable to or even higher than previously demonstrated Si- and TiO_2-based structural color metasurfaces[22,41,65]. In addition, the full width at half maximum (FWHM) values of the main peaks for all samples are narrower than ≈20 nm, suggesting high purity of the achieved colors. We calculate the color coordinates from both the simulated and measured spectra, and plotted the coordinates in the CIE 1931 XYZ chromaticity diagram (Section VI, Supplementary Information). Furthermore, we implement color printing of words "META" and "NIST" utilizing four different metasurface structures with lattice spacings respectively set as 280 nm, 340 nm, 360 nm, and 400 nm. When the samples are illuminated with a white light under bright-field microscope, images with each constituent letter of uniform and vivid color can be clearly observed (Fig. 4d).

Discussion

In conclusion, we present a new dielectric material platform based on tantalum pentoxide (Ta_2O_5), for realizing high-efficiency metasurface optics over the UV and visible spectrum. Ta_2O_5 is characterized by a wide bandgap value of ≈4.0 eV, enabling low-loss metasurface operation across the whole visible and near-UV regions, as well as part of the mid-UV region. Moreover, the material can be easily deposited uniformly onto various substrates over large areas using simple physical vapor deposition and patterned into high-aspect-ratio nanostructures through common fluorine-gas-based reactive ion etching. We demonstrate an array of high-performance UV and visible Ta_2O_5 metasurfaces with representative wavefront shaping capabilities, namely, polarization-independent UV metalenses of focusing efficiencies up to 65%, spin-selective metaholograms operating in the near-UV and blue spectrum with peak efficiencies exceeding 75%, and full-visible-region structural color generating Mie resonators exhibiting peak reflection intensities close to 80%. Thanks to this versatile material platform, these devices, though based on conventional designs, already exhibit performance that is comparable to state-of-the-art UV and visible metasurfaces using other dielectric materials. We believe their performance can be further improved by advanced metasurface design strategies, such as topology optimization[66] and machine learning[67]. Our work offers a new vista for realizing low-loss and fabrication-friendly dielectric metasurfaces operating in the UV and visible regions, enabling various applications such as atom trapping, high-resolution imaging, and advanced display with a compact form factor.

Materials and Methods

Film thickness and refractive index characterization

The Ta_2O_5 layer is sputter-deposited onto a silicon wafer coated with a 300 nm thick thermal oxide layer. The film's refractive index and thickness value are characterized by reflection-mode spectroscopic ellipsometry using the interference enhancement method[68,69], at three different angles of incidence (55°, 65°, and 75°) with respect to the normal to the plane of the Ta_2O_5 layer.

Metalens characterization

To characterize the metalenses, a continuous wave (CW) Helium–Cadmium (HeCd) laser ($\lambda_0 = 325$ nm) is employed to illuminate each sample at normal incidence. The intensity distribution on the lens focal plane is captured using a custom-built imaging system including an NA = 0.75 objective and an electron multiplying charge-coupled device (EMCCD) camera. The system magnification, characterized by translating the focal spot within the field of view of the objective using a high-precision motorized stage, is measured to be ≈546 (for $L_{325}^{0.5}$), ≈548 (for $L_{325}^{0.55}$), ≈550 (for $L_{325}^{0.6}$), and ≈547 (for $L_{325}^{0.7}$). The physical size of the focal spot projected by each metalens is derived based on the calibrated magnification and the pixel size of the EMCCD.

Metahologram characterization

To characterize the metahologram, a CW HeCd laser ($\lambda_0 = 325$ nm) is employed to illuminate the sample at normal incidence. A pair of linear polarizer and half-waveplate is used to convert the state of polarization of the incident beam to LCP. An EMCCD camera is placed in the plane of the holographic image to directly record the projected holographic image.

Acknowledgements

L. C., Z. W. and W. Z. acknowledge the support under the Cooperative Research Agreement between the University of Maryland and the National Institute of Standards and Technology (NIST) Physical Measurement Laboratory, Award No. 70NANB14H209, through the University of Maryland. O. K. was supported by an appointment to the Intelligence Community Postdoctoral Research Fellowship

Program at NIST administered by Oak Ridge Institute for Science and Education (ORISE) through an interagency agreement between the U.S. Department of Energy and the Office of the Director of National Intelligence (ODNI). C. Z. acknowledges the assistance from Ms. Yuhui Hu and Mr. Zhenyu Xing during the manuscript preparation process. All authors acknowledge Prof. Mu Ku Chen, Prof. Arka Majumdar and Prof. Kun Huang for kindly providing the refractive index data of GaN, SiN_x, and Nb_2O_5, respectively. Certain commercial equipment and software are identified in this documentation to describe the subject adequately. Such identification does not imply recommendation or endorsement by the NIST, nor does it imply that the equipment identified is necessarily the best available for the purpose.

Author details
[1]School of Optical and Electronic Information & Wuhan National Laboratory for Optoelectronics, Huazhong University of Science and Technology, Wuhan, Hubei 430074, China. [2]National Institute of Standards and Technology, Gaithersburg, MD 20899, USA. [3]University of Maryland, College Park, MD 20742, USA. [4]National Institute of Standards and Technology, Boulder, CO 80305, USA

Author contributions
The project was initiated by C. Z., W. Z., D. C., H. J. L., S. P. and A. A. The device fabrication and characterization were performed by J. S., W. Z., Z. L., L. C., Z. W., D. C., G. S., C. Z. and A. A. The device design and simulation were performed by C. Z., Z. L., D. W., M. L., W. Z., H. J. L and A. A. All authors contributed to the interpretation of results and participated in the manuscript preparation.

Data availability
The data that support the plots within this paper and other finding of this study are available from the corresponding authors upon request.

Conflict of interest
The authors declare no competing interests.

Supplementary information The online version contains supplementary material available at https://doi.org/10.1038/s41377-023-01330-z.

Received: 7 August 2023 Revised: 22 October 2023 Accepted: 6 November 2023
Published online: 22 January 2024

References

1. Yu, N. F. & Capasso, F. Flat optics with designer metasurfaces. *Nat. Mater.* **13**, 139–150 (2014).
2. Ma, Q. et al. Directly wireless communication of human minds via non-invasive brain-computer-metasurface platform. *eLight* **2**, 11 (2022).
3. Sun, S. L. et al. Electromagnetic metasurfaces: physics and applications. *Adv. Opt. Photonics* **11**, 380–479 (2019).
4. Wang, D. Y. et al. Structural color generation: from layered thin films to optical metasurfaces. *Nanophotonics* **12**, 1019–1081 (2023).
5. Neshev, D. & Aharonovich, I. Optical metasurfaces: new generation building blocks for multi-functional optics. *Light Sci. Appl.* **7**, 58 (2018).
6. Li, L. L. et al. Intelligent metasurfaces: control, communication and computing. *eLight* **2**, 7 (2022).
7. Ding, F., Pors, A. & Bozhevolnyi, S. I. Gradient metasurfaces: a review of fundamentals and applications. *Rep. Prog. Physics* **81**, 026401 (2018).
8. Zhu, R. C. et al. Remotely mind-controlled metasurface via brainwaves. *eLight* **2**, 10 (2022).
9. Yin, S. X., Galiffi, E. & Alù, A. Floquet metamaterials. *eLight* **2**, 8 (2022).
10. Zhu, Y. et al. Metasurfaces designed by a bidirectional deep neural network and iterative algorithm for generating quantitative field distributions. *Light: Adv. Manuf.* **4**, 104–114 (2023).
11. Chen, H. T., Taylor, A. J. & Yu, N. F. A review of metasurfaces: physics and applications. *Rep. Prog. Physics* **79**, 076401 (2016).
12. Kamali, S. M. et al. A review of dielectric optical metasurfaces for wavefront control. *Nanophotonics* **7**, 1041–1068 (2018).
13. Zhao, D. et al. Recent advances in ultraviolet nanophotonics: from plasmonics and metamaterials to metasurfaces. *Nanophotonics* **10**, 2283–2308 (2021).
14. Rybin, M. V. et al. High-*Q* supercavity modes in subwavelength dielectric resonators. *Phys. Rev. Lett.* **119**, 243901 (2017).
15. Zhang, X. F. et al. Metasurfaces for manipulating terahertz waves. *Light: Adv. Manuf.* **2**, 148–172 (2021).
16. Liu, K. et al. Active tuning of electromagnetically induced transparency from chalcogenide-only metasurface. *Light: Adv. Manuf.* **2**, 251–261 (2021).
17. Khorasaninejad, M. et al. Metalenses at visible wavelengths: diffraction-limited focusing and subwavelength resolution imaging. *Science* **352**, 1190–1194 (2016).
18. Liang, H. W. et al. Ultrahigh numerical aperture metalens at visible wavelengths. *Nano Lett.* **18**, 4460–4466 (2018).
19. Lin, R. J. et al. Achromatic metalens array for full-colour light-field imaging. *Nat. Nanotechnol.* **14**, 227–231 (2019).
20. Li, T. et al. Revolutionary meta-imaging: from superlens to metalens. *Photonics Insights* **2**, R01 (2023).
21. Zheng, G. X. et al. Metasurface holograms reaching 80% efficiency. *Nat. Nanotechnol.* **10**, 308–312 (2015).
22. Yang, W. H. et al. All-dielectric metasurface for high-performance structural color. *Nat. Commun.* **11**, 1864 (2020).
23. Li, Y. et al. Ultracompact multifunctional metalens visor for augmented reality displays. *PhotoniX* **3**, 29 (2022).
24. Liu, Z. Y. et al. Metasurface-enabled augmented reality display: a review. *Adv. Photonics* **5**, 034001 (2023).
25. Zhang, S. Y. et al. Metasurfaces for biomedical applications: imaging and sensing from a nanophotonics perspective. *Nanophotonics* **10**, 259–293 (2020).
26. Arbabi, E. et al. Full-stokes imaging polarimetry using dielectric metasurfaces. *ACS Photonics* **5**, 3132–3140 (2018).
27. Ni, Y. B. et al. Computational spectropolarimetry with a tunable liquid crystal metasurface. *eLight* **2**, 23 (2022).
28. Wang, K. et al. Quantum metasurface for multiphoton interference and state reconstruction. *Science* **361**, 1104–1108 (2018).
29. Li, L. et al. Metalens-array-based high-dimensional and multiphoton quantum source. *Science* **368**, 1487–1490 (2020).
30. Wang, K., Chekhova, M. & Kivshar, Y. Metasurfaces for quantum technologies. *Phys. Today* **75**, 38–44 (2022).
31. Arbabi, A. et al. Dielectric metasurfaces for complete control of phase and polarization with subwavelength spatial resolution and high transmission. *Nat. Nanotechnol.* **10**, 937–943 (2015).
32. Ako, R. T. et al. Dielectrics for terahertz metasurfaces: material selection and fabrication techniques. *Adv. Opt. Mater.* **8**, 1900750 (2020).
33. Divitt, S. et al. Ultrafast optical pulse shaping using dielectric metasurfaces. *Science* **364**, 890–894 (2019).
34. Colburn, S., Zhan, A. L. & Majumdar, A. Metasurface optics for full-color computational imaging. *Sci. Adv.* **4**, eaar2114 (2018).
35. Fan, Z. B. et al. Silicon nitride metalenses for close-to-one numerical aperture and wide-angle visible imaging. *Phys. Rev. Appl.* **10**, 014005 (2018).
36. Colburn, S. et al. Broadband transparent and CMOS-compatible flat optics with silicon nitride metasurfaces [Invited]. *Opt. Mater. Express* **8**, 2330–2344 (2018).
37. Wang, S. M. et al. A broadband achromatic metalens in the visible. *Nat. Nanotechnol.* **13**, 227–232 (2018).
38. Chen, B. H. et al. GaN metalens for pixel-level full-color routing at visible light. *Nano Lett.* **17**, 6345–6352 (2017).
39. Devlin, R. C. et al. Broadband high-efficiency dielectric metasurfaces for the visible spectrum. *Proc. Natl Acad. Sci. USA* **113**, 10473–10478 (2016).
40. Chen, W. T. et al. A broadband achromatic metalens for focusing and imaging in the visible. *Nat. Nanotechnol.* **13**, 220–226 (2018).
41. Sun, S. et al. All-dielectric full-color printing with TiO_2 metasurfaces. *ACS Nano* **11**, 4445–4452 (2017).
42. Zhang, C. et al. Low-loss metasurface optics down to the deep ultraviolet region. *Light Sci. Appl.* **9**, 55 (2020).
43. Huang, K. et al. Ultraviolet metasurfaces of ≈80% efficiency with antiferromagnetic resonances for optical vectorial anti-counterfeiting. *Laser Photonics Rev.* **13**, 1800289 (2019).
44. Gao, X. et al. Design of AlN ultraviolet metasurface for single-/multi-plane holography. *Appl. Opt.* **59**, 4398–4403 (2020).
45. Hu, Z. L. et al. Ultrawide bandgap AlN metasurfaces for ultraviolet focusing and routing. *Opt. Lett.* **45**, 3466–3469 (2020).
46. Kim, J. et al. One-step printable platform for high-efficiency metasurfaces down to the deep-ultraviolet region. *Light Sci. Appl.* **12**, 68 (2023).

47. Gil, B. et al. Boron nitride for excitonics, nano photonics, and quantum technologies. *Nanophotonics* **9**, 3483–3504 (2020).
48. Grudinin, D. V. et al. Hexagonal boron nitride nanophotonics: a record-breaking material for the ultraviolet and visible spectral ranges. *Mater. Horizons* **10**, 2427–2435 (2023).
49. Kühner, L. et al. High-*Q* nanophotonics over the full visible spectrum enabled by hexagonal boron nitride metasurfaces. *Adv. Materi.* **35**, 2209688 (2023).
50. Zotev, P. G. et al. Van der Waals materials for applications in nanophotonics. *Laser Photon. Rev.* **17**, 2200957 (2023).
51. Semmlinger, M. et al. Vacuum ultraviolet light-generating metasurface. *Nano Lett.* **18**, 5738–5743 (2018).
52. Tseng, M. L. et al. Vacuum ultraviolet nonlinear metalens. *Sci. Adv.* **8**, eabn5644 (2022).
53. Li, J. et al. Resonance-free ultraviolet metaoptics via photon nanosieves. *Opt. Lett.* **44**, 3418–3421 (2019).
54. Ossiander, M. et al. Extreme ultraviolet metalens by vacuum guiding. *Science* **380**, 59–63 (2023).
55. Steinlechner, J. Development of mirror coatings for gravitational-wave detectors. *Philos. Trans. Royal Soc. A* **376**, 20170282 (2018).
56. MacFarlane, N. et al. Niobium-tantalum oxide as a material platform for linear and nonlinear integrated photonics. *Opt. Express* **30**, 42155–42167 (2022).
57. Jung, H. et al. Tantala Kerr nonlinear integrated photonics. *Optica* **8**, 811–817 (2021).
58. Black, J. A. et al. Group-velocity-dispersion engineering of tantala integrated photonics. *Opt. Lett.* **46**, 817–820 (2021).
59. Khorasaninejad, M. & Crozier, K. B. Silicon nanofin grating as a miniature chirality-distinguishing beam-splitter. *Nat. Commun.* **5**, 5386 (2014).
60. Lin, D. M. et al. Dielectric gradient metasurface optical elements. *Science* **345**, 298–302 (2014).
61. Gerchberg, R. W. & Saxton, W. O. A practical algorithm for the determination of phase from image and diffraction plane pictures. *Optik* **35**, 237–246 (1972).
62. Baek, K. et al. Mie resonant structural colors. *ACS Appl. Mater. Interfaces* **12**, 5300–5318 (2020).
63. Proust, J. et al. All-dielectric colored metasurfaces with silicon Mie resonators. *ACS Nano* **10**, 7761–7767 (2016).
64. Yang, B. et al. Structural colors in metasurfaces: principle, design and applications. *Mater. Chem. Front.* **3**, 750–761 (2019).
65. Yang, B. et al. Ultrahighly saturated structural colors enhanced by multipolar-modulated metasurfaces. *Nano Lett.* **19**, 4221–4228 (2019).
66. Phan, T. et al. High-efficiency, large-area, topology-optimized metasurfaces. *Light Sci. Appl.* **8**, 48 (2019).
67. An, S. S. et al. A deep learning approach for objective-driven all-dielectric metasurface design. *ACS Photonics* **6**, 3196–3207 (2019).
68. Hilfiker, J. N. et al. Survey of methods to characterize thin absorbing films with spectroscopic ellipsometry. *Thin Solid Films* **516**, 7979–7989 (2008).
69. Zhang, C. et al. Robust extraction of hyperbolic metamaterial permittivity using total internal reflection ellipsometry. *ACS Photonics* **5**, 2234–2242 (2018).